Unconventional magnetic states and defects

Barts, Evgenii

DOI:
10.33612/diss.784926551

Chapter 3

Magnetic particles and strings in iron langasite

Abstract

Magnetic topological defects can store and carry information. Replacement of extended defects, such as domain walls and Skyrmion tubes, by compact magnetic particles that can propagate in all three spatial directions may open an extra dimension in the design of magnetic memory and data processing devices. We show[1] that such objects can be found in iron langasite, which exhibits a hierarchy of non-collinear antiferromagnetic spin structures at very different length scales. We derive an effective model describing long-distance magnetic modulations in this chiral magnet and find unusual two- and three-dimensional topological defects. The order parameter space of our model is similar to that of superfluid ^{3}He-A, and the particle-like magnetic defect is closely related to the Shankar monopole and hedgehog soliton in the Skyrme model of baryons. Mobile magnetic particles stabilized in non-collinear antiferromagnets can play an important role in antiferromagnetic spintronics.

3.1 Introduction

The topology of defects in ordered states of matter is governed by the order parameter describing spontaneous symmetry breaking at a phase transition [4]. As the number of variables required to characterize an ordered state increases, so does the diversity and complexity of topological defects. A wide variety of defects is found in superfluid ^{3}He with the order parameter describing orbital momentum, spin, and phase of the condensate [87, 88].

Nontrivial topology does not necessarily make defects stable: a competition between interactions with different properties under the scaling transformation, $\mathbf{x} \to \Lambda\mathbf{x}$, is required to prevent the collapse of the defect [51]. Thus isolated Skyrmion tubes in chiral magnets with a diameter of 10-100 nm are stabilized by Dzyaloshinskii-Moriya

[1] Barts, E., Mostovoy, M. Magnetic particles and strings in iron langasite. *npj Quantum Mater.* **6**, 104 (2021)

(DM) interactions [38, 39] favoring non-collinear spins, which compete with the Zeeman and magnetic anisotropy energy favoring uniform states [1, 36, 37]. The small size and high stability of Skyrmion tubes in bulk chiral magnets and magnetic multilayers, as well as their dynamics, driven by applied electric currents, make them promising information carriers in magnetic memory and data processing devices [2, 3, 5]. Even smaller skyrmions have been recently observed in centrosymmetric magnets [43–45], where they are stabilized by magnetic frustration and/or long-ranged interactions between spins mediated by conduction electrons [40, 41, 89–91].

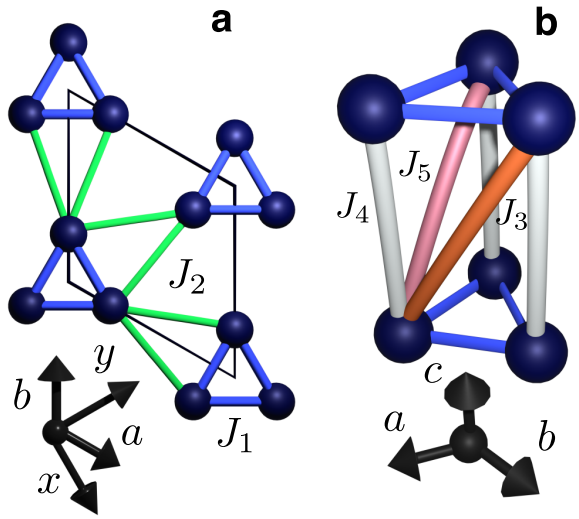

Figure 3.1: ***The Fe-langasite crystal structure.*** **a** *Spin triangles in the crystallographic ab plane formed by* Fe^{3+} *ions (blue spheres). Blue lines mark the bonds between the spins in the triangles with the relatively strong AFM exchange interaction* J_1*. The triangles form a hexagonal lattice with the AFM coupling* J_2 *between the triangles.* **b** *Stacking of the spin triangles along the c axis with the competing AFM interactions* J_3, J_4*, and* J_5 *between the spins in neighboring triangles.*

Here, we discuss a realistic material that can host three-dimensional (3D) magnetic Skyrmions – non-singular defects which, unlike the Skyrmion tubes, have a finite size in all three spatial directions. These magnetic particles can transfer information in all directions, stimulating the design of three-dimensional spintronic devices. 3D Skyrmions originally emerged as solitons in the non-linear meson model of T.H.R. Skyrme [10]. The parameter space of this model, formed by four meson fields, is three-sphere S^3 parametrized by three angles. A closely related defect, Shankar monopole, was predicted to exist in the A-phase of superfluid ^{3}He [11, 12]. The order parameter describing this phase is an SO(3) matrix, and the collection of all possible

ordered states is projective three-sphere RP^3. Shankar monopole has been recently realized in the Bose-Einstein condensate of trapped spin-1 particles by application of time-dependent and spatially inhomogeneous magnetic fields [92]. This defect is, however, unstable and has a short lifetime.

Higher-dimensional order parameter spaces can also be realized in magnetic materials, in particular, antiferromagnets with triangle-based spin lattices showing a non-collinear 120° ordering of spins in the triangles described by an SO(3) matrix [93, 94]. Non-collinear antiferromagnetic (AFM) orders give rise to electron and magnon bands with non-trivial topology and Weyl fermions [95–99] resulting in large anomalous Hall and Nernst effects [100, 101] that can be controlled electrically [102].

We show that 3D skyrmions can naturally occur in the iron langasite, $Ba_3TaFe_3Si_2O_{14}$. This fascinating material is both magnetically frustrated and chiral. The Fe-langasite spin lattice is built of triangles formed by the Fe^{3+}-ions in the *ab* layers (see Fig. 3.1) with AFM Heisenberg exchange interactions between spins in the triangles resulting in a 120° spin ordering [103]. Furthermore, competing exchange interactions between spins of neighboring triangles, stacked along the c axis, give rise to a helical spiral modulation of the 120°-ordering with the period of ~ 7 lattice constants along the c axis. The direction of the spin rotation in the spiral is governed by the chiral nature of the langasite crystal [103–106] that, otherwise, has little effect on the spin structure. However, when the magnetic anisotropy is effectively reduced by an applied magnetic field, DM interactions give rise to an additional spiral modulation with a period of about 2000 Å along a direction perpendicular to the c axis [107]. We show that the same DM interactions can stabilize more complex modulated states as well as unusual topological magnetic defects, in particular, the magnetic particles carrying 3D Skyrmion topological charge and an associated Hopf number.

3.2 Effective model

The 120° order of the classical unit spins $\mathbf{S}_1, \mathbf{S}_2, \mathbf{S}_3$ in triangles can be described by two orthogonal unit vectors, $\mathbf{V}_1$ and $\mathbf{V}_2$ [107, 108]: $\mathbf{S}_1 = \mathbf{V}_1$, $\mathbf{S}_2 = -\frac{1}{2}\mathbf{V}_1 + \frac{\sqrt{3}}{2}\mathbf{V}_2$ and $\mathbf{S}_3 = -\frac{1}{2}\mathbf{V}_1 - \frac{\sqrt{3}}{2}\mathbf{V}_2$, so that $\mathbf{S}_1 + \mathbf{S}_2 + \mathbf{S}_3 = 0$. Spatial rotations of the frame formed by $\mathbf{V}_1$, $\mathbf{V}_2$ and $\mathbf{n} = \mathbf{V}_1 \times \mathbf{V}_2$ are described by SO(3) matrix R parametrized by three Euler angles, ϕ, θ and Ψ [109]:

$$\mathbf{V}_{1,2} = R\mathbf{V}_{1,2}^{(0)} = R_z(\phi)R_y(\theta)R_z(\Psi)\,\mathbf{V}_{1,2}^{(0)}, \tag{3.1}$$

where R_z and R_y are the matrices of rotations around the z and y axes, respectively,

$$R_z(\Psi) = \begin{pmatrix} \cos\Psi & -\sin\Psi & 0 \\ \sin\Psi & \cos\Psi & 0 \\ 0 & 0 & 1 \end{pmatrix}, \quad R_y(\theta) = \begin{pmatrix} \cos\theta & 0 & \sin\theta \\ 0 & 1 & 0 \\ -\sin\theta & 0 & \cos\theta \end{pmatrix}, \tag{3.2}$$

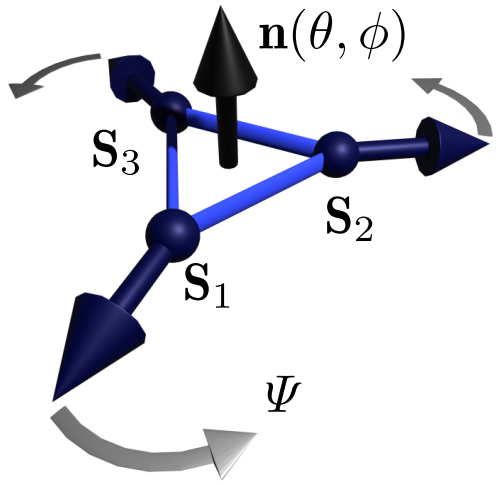

Figure 3.2: ***The 120° spin order.*** *The order parameter is described by the polar and azimuthal angles, θ and ϕ, of the vector chirality* $\mathbf{n} = \frac{2}{3\sqrt{3}}(\mathbf{S}_1 \times \mathbf{S}_2 + \mathbf{S}_2 \times \mathbf{S}_3 + \mathbf{S}_3 \times \mathbf{S}_1)$*, and the angle Ψ of the spin rotation around* $\mathbf{n}$.

θ and ϕ are the polar and azimuthal angles of the unit vector

$$\mathbf{n} = (\sin\theta\cos\phi, \sin\theta\sin\phi, \cos\theta)^T \tag{3.3}$$

describing the direction of the vector chirality of the 120° spin order (see Fig. 3.2), $\mathbf{V}_1^{(0)} = \hat{\mathbf{x}}$ and $\mathbf{V}_2^{(0)} = \hat{\mathbf{y}}$.

The short-period spiral ordering observed in Fe-langasite in zero magnetic field originates from the competing exchange interactions between the spin triangles stacked along the c direction (see Fig. 3.1 **b**). Importantly, the isotropic Heisenberg exchange interactions determine the spiral wave vector $Q \| c$ [104]:

$$\tan Qc = \sqrt{3}\frac{(J_5 - J_3)}{(2J_4 - J_3 - J_5)}, \tag{3.4}$$

but not the orientation of the spiral plane described by the vector chirality $\mathbf{n}$. The latter is governed by DM interactions between spins in the triangles,

$$D_z\left(\mathbf{S}_1 \times \mathbf{S}_2 + \mathbf{S}_2 \times \mathbf{S}_3 + \mathbf{S}_3 \times \mathbf{S}_1\right)_z = \frac{3\sqrt{3}}{2} D_z n_z, \tag{3.5}$$

favoring a helical spiral with the helicity $\mathrm{sign}(n_z Q)$ [103] and by an easy-plane magnetic anisotropy, which are two orders of magnitude weaker than the exchange interaction in the triangles [105, 106, 110]. On the other hand, the inter-triangle DM interactions

in this chiral magnet tend to induce 'slow' variations of $\mathbf{n}$ and Ψ giving rise to a long-period magnetic superstructure observed under an applied magnetic field [107]. The competition between the magnetic anisotropy favoring a unique direction of $\mathbf{n}$ and the tendency to large-scale modulations, both being relatively weak relativistic effects, can also stabilize topological magnetic defects that are superimposed on the fast spin rotations with the propagation vector along the c direction.

To obtain an effective model describing long-period magnetic superstructures in Fe-langasite, we separate fast and slow variations of the order parameter by introducing a slowly varying angle $\psi(\mathbf{r})$:

$$\Psi(\mathbf{r}) = Qz + \psi(\mathbf{r}). \tag{3.6}$$

The energy is then expanded in powers of gradients of the three slowly varying angles θ, ϕ and ψ, and averaged over the fast spin rotations (technical details of the derivation can be found in Appendix 3.9.2). The energy density of the effective model is

$$\begin{aligned}\mathcal{E} = {} & \frac{J_z}{2}\Big[(\partial_z \mathbf{n})^2 + 2(D_z\psi)^2\Big] + \frac{J_\perp}{2}\sum_{\mu=x,y}\Big[(\partial_\mu \mathbf{n})^2 + 2(D_\mu\psi)^2\Big] \\ & + K_1(1-\cos\theta) + \frac{K_2}{2}(1-\cos^2\theta) - \frac{\chi}{2}(\mathbf{H}\cdot\mathbf{n})^2 \\ & + \lambda\Big[\cos^2\theta(-\sin\phi\,\partial_x\theta + \cos\phi\,\partial_y\theta) + (\mathbf{n}\cdot\partial_\perp)\,\psi\Big],\end{aligned} \tag{3.7}$$

where the first term originates from the interlayer Heisenberg exchange interactions (see Fig. 3.1 **b**) and $J_z = \frac{3}{4}\sqrt{(2J_4 - J_3 - J_5)^2 + 3(J_3 - J_5)^2}$. The second term with $J_\perp = \frac{\sqrt{3}}{2}J_2$ results from the exchange interactions between the Fe-triangles in the ab layers (Fig. 3.1 **a**). The distances in the direction parallel(perpendicular) to the c axis of the hexagonal lattice are measured in units of the lattice constant, $c(a)$. $D_i\psi = \partial_i\psi + \cos\theta\,\partial_i\phi$ is the covariant derivative of ψ ($i = x, y, z$) invariant under an arbitrary global rotation of spins. The third term in Eq. (3.7), playing the role of an internal magnetic field, originates from DM interactions between spins in the triangles [see Eq.(3.5)] and the fourth term is the magnetocrystalline anisotropy. The next term is the coupling of the spiral ordering to an applied magnetic field $\mathbf{H}$, which favors $\mathbf{n} \parallel \mathbf{H}$ ($\chi > 0$) since the magnetic susceptibility is the largest for spins rotating in the plane perpendicular to the field vector. The last term in Eq. (3.7) is a Lifshitz invariant (LI) [1, 39] allowed by the chiral nature of the langasite crystal, $\partial_\perp$ being gradient along the in-plane directions.

Lifshitz invariants (LIs) for chiral antiferromagnets with a 120° spin order, such as swedenborgaties and langasites, can be written in terms of the two vectors, $\mathbf{V}_1$ and $\mathbf{V}_2$, and their derivatives. They can be easily found using one-dimensional complex representations of 3_z. To this end we introduce linear combinations of $\mathbf{V}_1 = (X_1, Y_1, Z_1)$

and $\mathbf{V}_2 = (X_2, Y_2, Z_2)$:

$$\begin{aligned} R_+ &= X_1 + iX_2 + i(Y_1 + iY_2) = \mathrm{e}^{\mathrm{i}(\phi - \Psi)}\,(\cos\theta - 1)\,, \\ R_- &= X_1 + iX_2 - i(Y_1 + iY_2) = \mathrm{e}^{-\mathrm{i}(\phi + \Psi)}\,(\cos\theta + 1)\,, \\ Z &= Z_1 + iZ_2 = -\sin\theta\,\mathrm{e}^{-\mathrm{i}\,\Psi}, \end{aligned} \tag{3.8}$$

and their complex conjugates denoted by $\bar{R}_+$, $\bar{R}_-$ and $\bar{Z}$, respectively. These quantities transform in a simple way under the generators of P321 group, 3_z and 2_y (see Table of Fig 3.3). These transformation rules follow directly from the symmetry properties of the order parameter:

$$\begin{aligned} &3_z : \phi \to \phi + \frac{2\pi}{3}, \quad \Psi \to \Psi - \frac{2\pi}{3}, \\ &2_y : \phi \to -\phi, \quad \Psi \to \pi - \Psi, \end{aligned} \tag{3.9}$$

and θ being invariant under these transformations.

	3_z	2_y
R_+	$\overline{\omega}$	$-\overline{R}_+$
$\overline{R}_+$	ω	$-R_+$
R_-	1	$-\overline{R}_-$
$\overline{R}_-$	1	$-R_-$
Z	ω	$-\overline{Z}$
$\overline{Z}$	$\overline{\omega}$	$-Z$

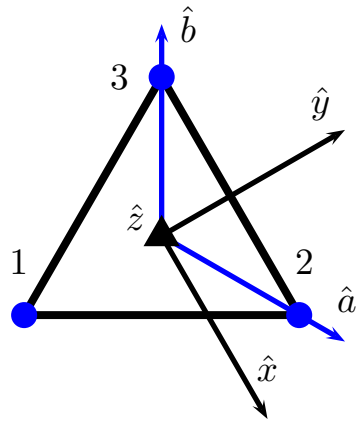

Figure 3.3: ***Transformation properties*** *of $R_\pm$, Z and their complex conjugates (see Eq.(3.8)) under the generators of P321 group, 3_z and 2_y. Here, $\omega = \mathrm{e}^{\mathrm{i}\frac{2\pi}{3}}$ and $\overline{\omega} = \mathrm{e}^{-\mathrm{i}\frac{2\pi}{3}}$. Guiding Fe-ions triangle shows the symmetry axes $\hat{z}$ and $\hat{y}$.*

Using these transformation properties, one obtains 5 independent LIs favoring an additional modulation with an in-plane wave: $\mathrm{Im}\left(R_+ \overleftrightarrow{\partial_+} R_-\right)$, $\mathrm{Im}\left(R_+ \overleftrightarrow{\partial_+} \overline{R}_-\right)$, $\mathrm{Im}\left(R_+ \overleftrightarrow{\partial_-} \overline{Z}\right)$, $\mathrm{Im}\left(R_- \overleftrightarrow{\partial_+} \overline{Z}\right)$, and $\mathrm{Im}\left(R_- \overleftrightarrow{\partial_-} Z\right)$, where $A \overleftrightarrow{\partial_\pm} B = A\partial_i B - B\partial_i A$ and $\partial_\pm = \partial_x \pm i\partial_y$. Two LIs vanish upon average over fast spin rotations [107]. Further details and the microscopic derivation of the LI from the DMI between nearest-neighbor triangles in the ab plane can be found in Appendix 3.9.3.

3.3 Phase diagram

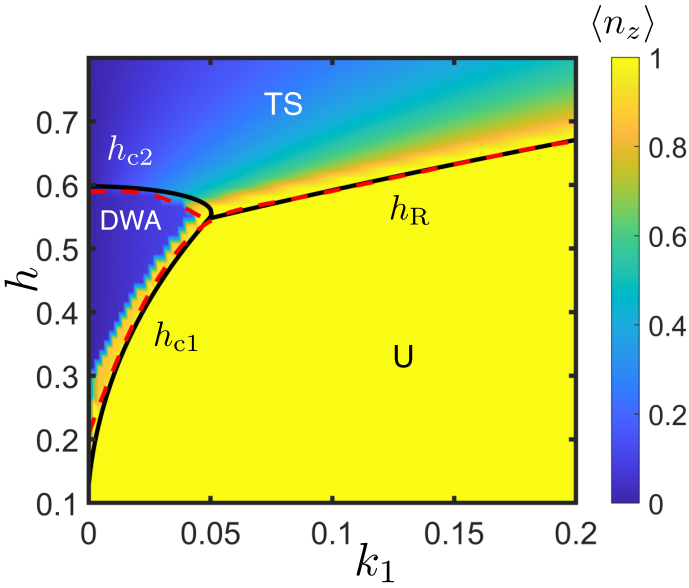

Figure 3.4: ***Magnetic phase diagram of the model.*** *The competing phases are: the 'uniform' (U) spiral state with $n \| z$ and $\psi = 0$, the modulated 'tilted spiral' (TS) state and the domain wall array (DWA). Solid black(dashed red) phase transition lines are obtained analytically(numerically), the difference being a finite-size effect in numerical calculations. Color indicates the average n_z. $k_{1,2} = K_{1,2}/\left(\frac{\lambda^2}{2J}\right)$ and the dimensionless magnetic field, h, is defined by $\chi H^2 = h^2 \frac{\lambda^2}{2J}$. This calculation was performed for $k_2 = 1.25$, $\lambda = 0.4$ and $J = 1.0$.*

In zero field, the anisotropy terms with $K_1, K_2 > 0$ confine spins to the ab plane and stabilize the spiral state called uniform (U), as in this state $n_z = +1$ and $\psi = \text{const}$. In enantiopure samples of Fe-langasite studied in experiments $n_z = -1$ [103–105]. The sign of n_z does not affect the phase diagram. An applied magnetic field $H \perp c$ tends to re-orient the spiral plane, eventually turning it perpendicular to the field ($n \| H$). The re-orientation of $\mathbf{n}$, which resembles the spin-flop transition in collinear antiferromagnets, activates LI that can stabilize two very different states with additional large-scale modulations.

Assuming that $\mathbf{n}$ and ψ in the modulated states vary along a vector $\xi = (\cos\phi_\xi, \sin\phi_\xi, 0)$ in the ab plane (this assumption is verified by numerical simulations), we exclude ψ from Eq.((3.7)) using $\partial_\xi \psi = -\cos\theta \partial_\xi \phi - \frac{\lambda}{2J_\perp}(\xi \cdot \mathbf{n})$ and obtain the energy that only

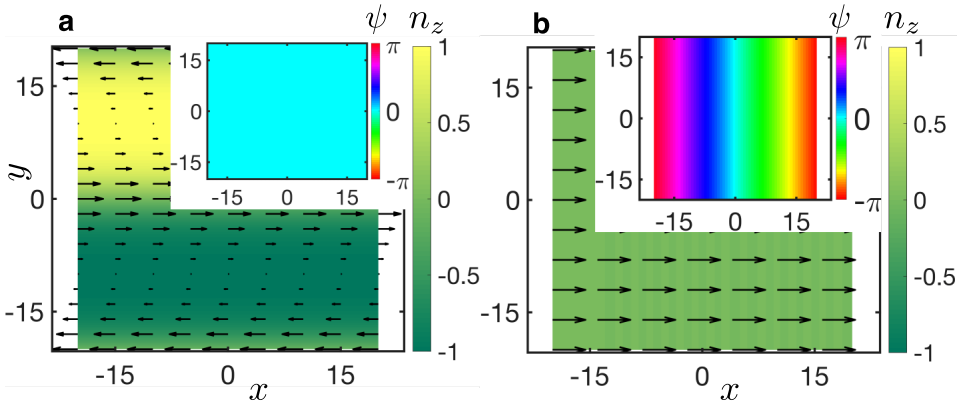

Figure 3.5: ***Modulated states induced by*** $H\|x$**.** **a** *The domain wall array, in which the angle* θ *rotates in the* xz *plane along the* y *axis normal to the field vector.* **b** *The 'tilted spiral' state with* $n\|H$ *and* ψ *varying along the field direction. The figures show the vector chirality* **n** *and the corresponding angle* ψ *is shown in the insets. In-plane components of* **n** *are indicated with arrows;* n_z *and* ψ *are color-coded.*

depends on **n**,

$$\mathcal{E} = \frac{J_\perp}{2}(\partial_\xi \mathbf{n})^2 + K_1(1-\cos\theta) + \frac{K_2}{2}(1-\cos^2\theta) \\ - \frac{\chi H^2}{2} n_x^2 - \frac{\lambda^2}{4J_\perp}(\xi\cdot\mathbf{n})^2 - \lambda \sin^2\theta \sin(\phi-\phi_\xi)\,\partial_\xi\theta, \tag{3.10}$$

for $H\|x$ (see the x direction in Fig. 3.1 **a** and Fig. 3.3).

Figure 3.4 shows the phase diagram in the (K_1, H) plane. In contrast to collinear antiferromagnets, the order parameter **n** does not abruptly flop, but rotates continuously away from the z axis in the xz plane. For $H > H_\mathrm{R}$: $\chi H_\mathrm{R}^2 = |K_1| + K_2 - \frac{\lambda^2}{2J_\perp}$, the rotation angle is given by

$$\cos\theta = \frac{K_1}{\chi H^2 + \frac{\lambda^2}{2J_\perp} - K_2}. \tag{3.11}$$

While **n** is constant, the angle ψ varies monotonically, $\psi = q(\mathbf{r}\cdot\xi)$ with $q = -\frac{\lambda}{2J_\perp}\sin\theta$, corresponding to an additional rotation of spins around **n** (see Fig. 3.5 **b**) recently observed in Fe-langasite above $H_\mathrm{R} \sim 4$ T [107]. The wave vector q increases as the field strength grows and **n** approaches the field direction. This 'tilted spiral' (TS) state with **n** tilted away from the c axis has both helical and cycloidal components.

In another kind of modulated state, the domain wall array (DWA) shown in Fig. 3.5 **a**, ψ is constant whereas **n** rotates in the xz plane along the y axis perpendicular to

the applied field ($\phi - \phi_\xi = \frac{\pi}{2}$). This state only appears for relatively small K_1 (see Fig. 3.4). At a critical field, H_{c1}, the energy of the domain wall, across which θ varies by 2π, vanishes, which marks the transition from the uniform spiral state to the DWA state. As H increases further, the domain wall energy becomes negative, and the domain walls form an array with the period that decreases with the field. This state is similar to the 'mixed state' in collinear antiferromagnets [111], except that in our case $\mathbf{n}$ rotates through the angle 2π across the wall, since the uniform states with $n_z = \pm 1$ have different energies for $K_1 \neq 0$. At the second critical field, H_{c2}, the transition between the DWA and TS states occurs and the modulation direction described by ξ rotates abruptly through 90°.

Although the energy of all states in the phase diagram Fig. 3.4 can be found analytically (see Appendix 3.9.4), we also performed numerical simulations of the model Eq. (3.7) re-written in terms of two orthogonal unit vectors, $\mathbf{V}_1$ and $\mathbf{V}_2$ (see Appendix 3.9.1), which confirm the phase diagram Fig. 3.4. We also found metastable multiply-periodic states: the vortex array with a square lattice (Fig. 3.6 **a**,**b**), the vortex chains (Fig. 3.6 **c**,**d**) and the hexagonal crystal of coreless vortices (Fig. 3.6 **e**,**f**), which can be stabilized by thermal fluctuations at elevated temperatures.

3.4 Topological magnetic defects in two spatial dimensions

Singular topological defects in a model with an SO(3) order parameter in two spatial dimensions – Z_2 vortices with energy logarithmically diverging with the system size – have been discussed in Ref. [93]. Here we study non-singular finite-energy defects in the uniform ground state. One might think that, similarly to magnetic Skyrmions, such defects can be classified by the topology of $\mathbf{n}(x, y)$-textures after the angle ψ is integrated out from Eq. (3.7), as it was done for one-dimensional states. However, in two spatial dimensions, the resulting energy functional, $E[\mathbf{n}]$, contains long-ranged Coulomb interactions between the 'electric' charges induced by spatial variations of $\mathbf{n}$. These interactions suppress Skyrmions, which are 'charged' and have an infinite 'electrostatic' energy.

The electrostatic potential, $\varphi_{\rm el}$, is a variable dual to ψ,

$$D_\mu \psi + \frac{\lambda}{2J_\perp} n_\mu = -\epsilon_{\mu\nu} \partial_\nu \varphi_{\rm el}, \tag{3.12}$$

where $\epsilon_{\mu\nu}$ is the antisymmetric tensor ($\mu, \nu = x, y$). The divergence of the left-hand side is 0 as a result of the global gauge invariance: Eq. (3.7) is unchanged under $\psi \to \psi + \alpha$. The electrostatic potential satisfies Poisson equation, $-\triangle \varphi_{\rm el} = 4\pi \rho_{\rm el}$,

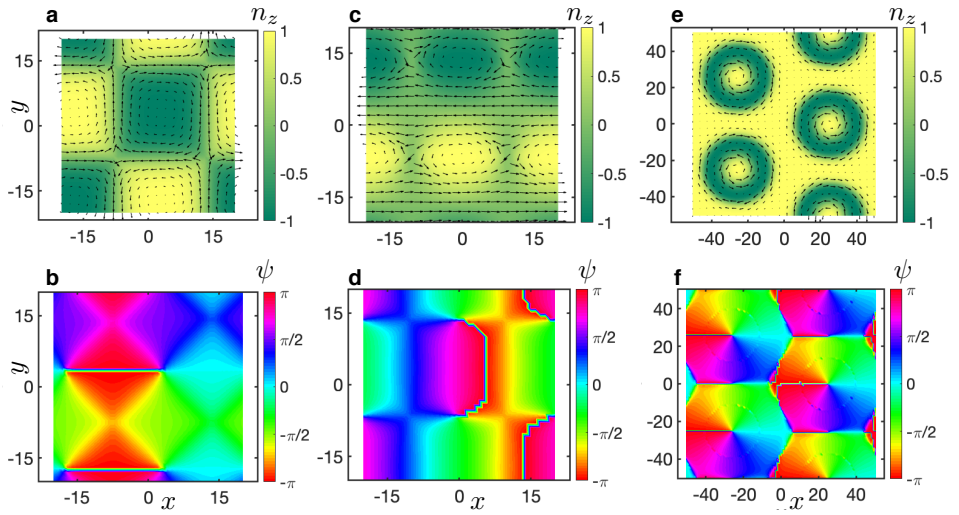

Figure 3.6: ***Metastable modulated states.*** **a**,**b** *The vortex array with a square lattice found at low applied magnetic fields ($H < H_R$).* **c**,**d** *The alternating strings of merons and antimerons found at large applied magnetic fields ($H > H_R$).* **e**,**f** *The non-singular hexagonal vortex crystal. The first row (panels* **a**,**c** *and* **e***) shows the vector chirality* **n** *and the second row (panels* **b**,**d** *and* **f***) shows the corresponding angle ψ. In-plane components of* **n** *are indicated with arrows; n_z and ψ are color-coded. The angle ψ is plotted modulo 2π and the lines in the ψ-plots are branch cuts, across which ψ discontinuously changes by 2π.*

with the electric charge density,

$$\rho_{\rm el} = \frac{1}{4\pi}(\mathbf{n}\cdot\partial_x\mathbf{n}\times\partial_y\mathbf{n}) - \frac{\lambda}{8\pi J_\perp}[\nabla\times\mathbf{n}]_z, \tag{3.13}$$

the first term being the Skyrmion charge density. Equation (3.7) can then be written in the form,

$$\mathcal{E} = \frac{J_\perp}{2}\sum_{\mu=x,y}(\partial_\mu\mathbf{n})^2 - \lambda n_z[\nabla\times\mathbf{n}]_z + U(\mathbf{n}) + \frac{1}{2\epsilon}\varphi_{\rm el}\rho_{\rm el}, \tag{3.14}$$

where $U(\mathbf{n}) = K_1(1-\cos\theta) + \frac{\left(K_2-\frac{\lambda^2}{2J_\perp}\right)}{2}\sin^2\theta - \frac{\chi}{2}(\mathbf{H}\cdot\mathbf{n})^2$ and the last term is the positive electrostatic energy with the 'dielectric' constant $\epsilon = \frac{1}{8\pi J_\perp}$. Finite-energy defects have zero total electric charge,

$$Q_{\rm el} = \int d^2x\rho_{\rm el} = Q_{\rm sk} - \frac{\lambda}{8\pi J_\perp}\oint d\mathbf{x}\cdot\mathbf{n} = 0, \tag{3.15}$$

where $Q_{\rm sk}$ is the Skyrmion charge (Eq.(3.15) is similar to the Mermin-Ho relation for the circulation of the superfluid velocity in ^{3}He-A [112]. Since for a finite-energy defect

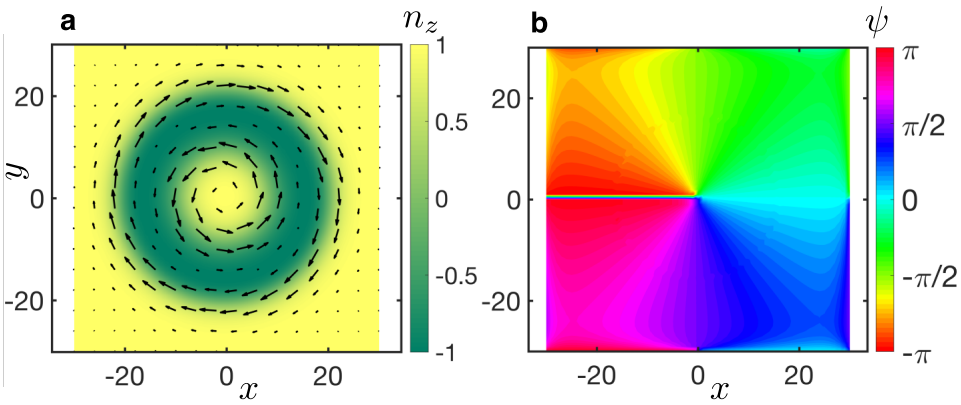

Figure 3.7: ***Coreless vortex in the uniform spiral state.*** *This topological defect consists of a target skyrmion formed by the vector chirality* $\mathbf{n}$ *(panel* **a***) and a vortex, in which the angle* ψ *varies by* -2π *along a closed loop around the center of the defect (panel* **b***). Arrows show in-plane components of* $\mathbf{n}$*;* n_z *and* ψ *are color-coded. The numerical simulation was done for* $J_\perp = 1, \lambda = 0.34, K_1 = 0, K_2 = 0.1$*, and* $\mathbf{H} = 0$*.*

the integral over the infinite-radius circle in Eq.(3.15) is 0, $Q_{\rm sk} = 0$, in agreement with $\pi_2(\mathrm{SO}(3)) = 0$.

A stable finite-energy defect in the spiral state with $n \| \hat{z}$ is shown in Fig. 3.7. In polar coordinates (ρ, φ), $\phi = \varphi + \frac{\pi}{2}$, $\psi = -\varphi$ and $\theta = \theta(\rho)$ monotonically increases from 0 at $\rho = 0$ to 2π at $\rho = \infty$. The $\mathbf{n}$-configuration shown in Fig. 3.7) **a** is that of a target skyrmion [113–115] with $Q_{\rm sk} = 0$ and the angle ψ forms a vortex with the winding number -1 (Fig. 3.7 **b**). As in the vortices in type-II superconductors, the covariant derivative $D_\mu \psi$ vanishes far away from the vortex. However, it also vanishes at $\rho = 0$, so that the ψ-vortex has no core. Note that $\phi + \psi = \text{const}$ in the vortex center, where $\theta = 0$, corresponds to non-rotating spins.

This defect is stabilized by the LI in Eq. (3.7), which favors ψ varying along $\mathbf{n}$ and θ varying along the direction normal to $\mathbf{n}$. Both these trends are fulfilled in the coreless vortex. Topological protection is ensured by the existence of a non-contractible loop in the SO(3) manifold: $\pi_1(\mathrm{SO}(3)) = Z_2$. A path from the center of the defect to infinity along any radial direction is such a loop. In the center of the defect and at spatial infinity $n_z = +1$, whereas inside the green ring in Fig. 3.7 **a** n_z is negative, corresponding to the reversal of both the vector chirality of spins in triangles and the spiral helicity. The rotational symmetry of the defect turns the calculation of $\theta(\rho)$ into a one-dimensional problem (see Appendix 3.9.5).

3.5 2D vortices in applied fields

Applied in-plane fields generate elliptical distortions of the two-dimensional vortex favored by Zeeman interaction. At the fields above critical, we did not find a similar finite energy defect. However, we found the singular bi-meron defects, which can be observed at the phase transition to the flopped spiral state. Figure 3.8 shows a topological defect in the double-helix state with $\boldsymbol{n}$ nearly parallel to the applied magnetic field $H \| x$ (above the flop transition). The $\boldsymbol{n}$-configuration has the form of a bi-meron pair (panel a). Both merons are ϕ-vortices with the winding number $+1$. $n_z = +1$ in the center of one meron and -1 in the center of the other. The merons have half-integer skyrmion charges of opposite sign (the total skyrmion charge of the defect is 0, in agreement with the discussion above). The center of the meron with $n_z = \pm 1$ is simultaneously the center of the ψ-vortex with the winding number ∓ 1, i.e., the ψ-configuration is that of vortex-antivortex pair (panel b). The logarithmic divergence of energy comes from two singular points of the boundary line between merons.

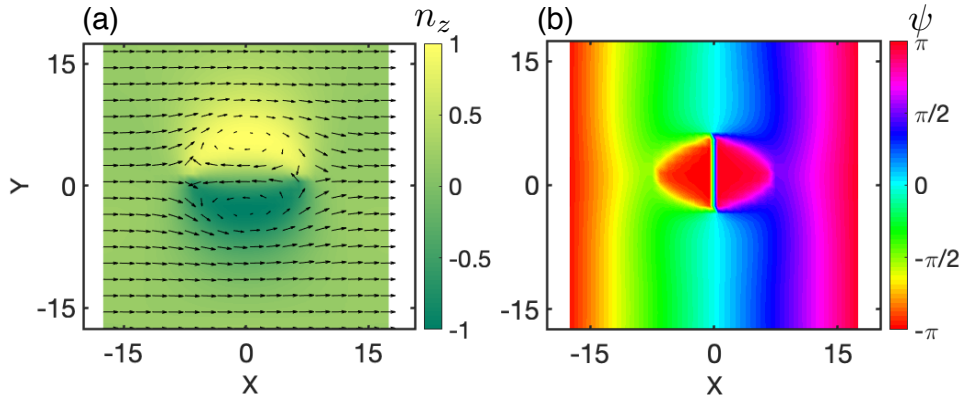

Figure 3.8: *Singular topological defect in the double-helix state with $\boldsymbol{n} \| \hat{\boldsymbol{x}}$. (a) The $\boldsymbol{n}$-configuration has the form of a bi-meron pair. The merons are vortices carrying with half-integer skyrmion charges of opposite sign. (b) The ψ-configuration has the form of a vortex-antivortex pair. Arrows show in-plane components of $\boldsymbol{n}$; n_z and ψ are color-coded. The numerical simulation was performed for $J_\perp = 1$, $\lambda = 0.2$, $K_1 = 0.01, K_2 = 0.1$, and $H_x = 0.25$.*

3.6 3D Skyrmion

The third homotopy group, $\pi_3\,(\mathrm{SO}(3)) = Z$, allows for particle-like topological defects that have a finite spatial extent in all three directions. They are closely related to

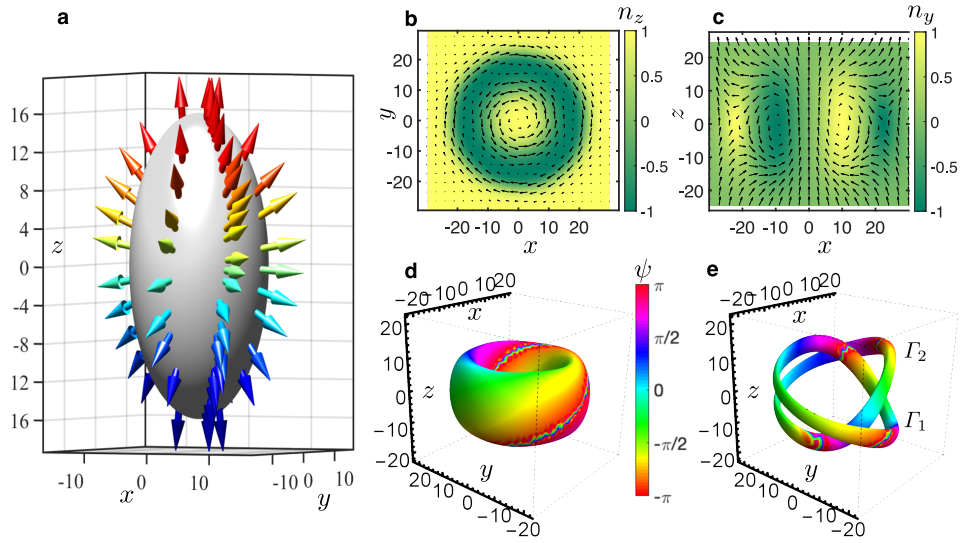

Figure 3.9: ***Three-dimensional Skyrmion in a thin layer of Fe-langasite.*** ***a*** *Arrows indicate the direction of* $\mathbf{\Phi} = (\Phi_x, \Phi_y, \Phi_z)$ *at the* $\Phi_0 = 0$ *surface (grey ellipsoid). The corresponding* **n***-configuration in the* xy *plane passing through* $z = 0$ *(panel* ***b****) and in the* xz *plane passing through* $y = 0$ *(panel* ***c****).* ***d*** *False color plot of the angle* ψ *at the* $n_z = -1/2$ *surface.* ***e*** *Linking of two closed oriented paths,* $\Gamma_{1,2}$*, formed by the constant-***n** *lines:* $\mathbf{n} = (0, \sqrt{3}/2, -1/2)^T$*, for* Γ_1*, and* $\mathbf{n} = (\sqrt{3}/2, 0, -1/2)^T$*, for* Γ_2*. The numerical simulation was done for* $J_\perp = J_z = 1, \lambda = 0.5, K_1 = 0, K_2 = 0.1$*,* $\mathbf{H} = 0$ *and an additional surface anisotropy with* $K_2^s(z) = 0.26 \cdot \exp(-\frac{(z_0 - |z|)}{3.0})$*, where* $z_0 = 25$ *is half-width of the film.*

hedgehog solitons in the non-linear meson model of T.H.R. Skyrme [10] carrying an integer topological charge identified with the baryon number,

$$\mathcal{H} = -\frac{1}{96\pi^2} \int d^3x \, \varepsilon_{ijk} \, \mathrm{tr}\big[L_i L_j L_k\big], \tag{3.16}$$

where ε_{ijk} is the antisymmetric Levi-Civita tensor ($i, j, k = x, y$ or z) and $L_i = U^\dagger \partial_i U$, U being an SU(2) matrix describing the four meson fields (Φ_0, Φ_x, Φ_y, Φ_z) on the 3-sphere ($\Phi_0^2 + \Phi_x^2 + \Phi_y^2 + \Phi_z^2 = 1$): $U = \Phi_0 \mathbb{1} + i\mathbf{\Phi} \cdot \sigma$, where $\sigma = (\sigma_x, \sigma_y, \sigma_z)$ is a vector composed of Pauli matrices. In the Skyrme's baryon, Φ_0 depends on the radius r, varying from -1 (the south pole of the 3-sphere) at $r = 0$ to $+1$ (the north pole) at infinity, and the vector $\mathbf{\Phi} = (\Phi_x, \Phi_y, \Phi_z)$ is along the radius vector $\mathbf{r}$ (a hedgehog), which guarantees that the 3-sphere formed by the meson fields wraps once around the three-dimensional Euclidean space. This configuration was used as the initial state for numerical studies of 3D topological excitations in the uniform spiral state.

The collapse of Skyrme's hedgehog is prevented by the terms of fourth order in

spatial derivatives of Φ^α. This stabilization mechanism is inefficient in Fe-langasite with relatively small fourth-order terms. 3D defects in chiral materials can be stabilized by DM interactions. The dependence of the 3D Skyrmion energy on the length scale R (for a fixed shape) is given by $E(R) = aR - bR^2 + cR^3$, where the first term is the positive exchange energy, the second term is the negative energy resulting from the LI, and the third term is the positive anisotropy energy counted from the energy of the uniform ground state ($a, b, c > 0$). The local minimum of $E(R)$ corresponding to a metastable Skyrmion appears for $b^2 > 3ac$.

Our numerical simulations with periodic boundary conditions in all three directions show that λ required to stabilize the 3D defect exceeds the critical value, above which the uniform spiral state becomes unstable towards additional periodic modulations, i.e., it transforms into the TS or DWA state in zero magnetic field. However, we have found a stable 3D Skyrmion in slabs with open boundary conditions along the z direction, periodic boundary conditions along the x and y directions, and a surface anisotropy favoring $\mathbf{n}$ (anti)parallel to the c axis, which suppresses the instability of the uniform state. This mechanism is similar to the stabilization of Hopfions in films of liquid crystals by boundary conditions [116].

Figure 3.9 **a** shows that the 3D Skyrmion is an axially symmetric hedgehog elongated along the c axis. The grey surface is a surface of $\Phi_0 = \cos\frac{\theta}{2}\cos\frac{\psi+\phi}{2} = 0$ and the arrows show the direction of $\mathbf{\Phi} = (\Phi_x, \Phi_y, \Phi_z) = (\sin\frac{\theta}{2}\sin\frac{\psi-\phi}{2}, \sin\frac{\theta}{2}\cos\frac{\psi-\phi}{2}, \cos\frac{\theta}{2}\sin\frac{\psi+\phi}{2})$ at this surface. $\Phi_0 = -1$ in the center of the 3D skyrmion and $\Phi_0 = +1$ at the periphery, so that the $\mathcal{H} = -1$ (see also Sec. 1.2.2).

The $\mathbf{n}$-configuration in the xy plane passing through the center of the defect is the 2D target skyrmion (Fig. 3.9 **b**), whereas the xz cut through the defect (see Fig. 3.9 **c**) shows a doughnut shape. In fact, the $\mathbf{n}$-part of the 3D skyrmion is a Hopfion, similar to Hopfions in ferromagnets and liquid crystals [22, 23, 117–119], and the 3D topological charge equals the Hopf number of the $\mathbf{n}$-texture written in terms of the vector potential $a_i = -D_i\psi = \mathbf{V}_1 \cdot \partial_i \mathbf{V}_2$ and the corresponding magnetic field $\mathbf{b} = [\nabla \times \mathbf{a}]$ [29, 31]:

$$\mathcal{H} = -\frac{1}{16\pi^2}\int d^3x\,(\mathbf{a}\cdot\mathbf{b}). \tag{3.17}$$

Figure 3.9 **d** shows the false-color plot of the angle ψ at the $n_z = -1/2$ surface (a torus). The angle ψ winds around the torus, which reflects the fact that Hopf number is the linking number for constant-$\mathbf{n}$ loops [31] (see Fig. 3.9 **e**). The change of the angle ψ along the loop, $\Delta\psi = -\oint d\mathbf{x}\cdot\mathbf{a} = -4\pi$. Importantly, the 3D Skyrmion is not merely a Hopfion, since the vector chirality $\mathbf{n}$ is only a part of the order parameter.

3.7 Variational solution of 3D skyrmion

To shed light on the stability properties of the isolated 3D skyrmion, we can analytically optimize its variational solution. The spherically symmetric skyrmion solution is parametrized with the angle $F = F(r)$:

$$\mathbf{\Phi} = \hat{\mathbf{r}} \sin F, \quad \Phi_0 = \cos F, \tag{3.18}$$

such that $F = \pi$ at the center of the skyrmion and $F = 0$ at the periphery. In terms of the $SO(3)$ order parameters, this solution can be conveniently written as [120]

$$\begin{aligned} n_x &= \sin 2F\, \hat{y} + (1 - \cos 2F)\, \hat{x}\hat{z}, \\ n_y &= -\sin 2F\, \hat{x} + (1 - \cos 2F)\, \hat{y}\hat{z}, \\ n_z &= \cos 2F\ + (1 - \cos 2F)\, \hat{z}^2, \end{aligned} \tag{3.19}$$

where $\hat{r}$ is one of the components of the radial unit vector, e.g., $\hat{z} = \frac{z}{r}$. The other Euler angles are

$$\phi = \varphi + \chi - \frac{\pi}{2}, \qquad \psi = -\varphi + \chi + \frac{\pi}{2}, \tag{3.20}$$

where χ winds around a circle of radius R in xy plane accumulating 2π along. The radius R is defined by the condition of $F(R) = \frac{\pi}{2}$. The shape of the $F(r)$ profile is the function to optimize. The energy functional of $\alpha(r) = 2F(r)$ is

$$E[\alpha] = 4\pi \int_0^\infty r^2 dr \left(\mathcal{E}_z + \mathcal{E}_{xy} + \mathcal{E}_{LI} + \mathcal{E}_{\mathrm{a}}\right). \tag{3.21}$$

The first term is exchange energy in z direction, $\mathcal{E}_z = \frac{J_\perp}{2}\left(A_2(\partial_r\alpha)^2 + \frac{2A_1}{r}(\partial_r\alpha) + \frac{A_0}{r^2}\right)$ with $A_2 = \frac{8}{15}$, $A_1 = \frac{2}{15}\sin\alpha$ and $A_0 = \frac{8}{15}\sin^2\alpha + \frac{4}{3}(1 - \cos\alpha)$. The second term is exchange energy in xy directions, $\mathcal{E}_{xy} = \frac{J_z}{2}\left(B_2(\partial_r\alpha)^2 + \frac{2B_1}{r}(\partial_r\alpha) + \frac{B_0}{r^2}\right)$ with $B_2 = \frac{4}{5}$, $B_1 = -\frac{2}{15}\sin\alpha$ and $B_0 = -\frac{8}{15}\sin^2\alpha + 4(1 - \cos\alpha)$. The third term is the contribution from the Lifshitz invariant, $\mathcal{E}_{LI} = \lambda\left(L_1(\partial_r\alpha) + \frac{L_0}{r}\right)$ with $L_1 = \frac{2}{15}\left(1 + 4\cos^2\alpha\right)$ and $L_0 = \frac{4}{3}\sin\alpha\left(1 - \frac{(1-\cos\alpha)}{5}\right)$. The last term in the energy is single-site anisotropy, $\mathcal{E}_{\mathrm{a}} = \frac{K_2}{2}\left(1 - < n_z^2 >\right)$ with $< n_z^2 >= \frac{1}{15}\left(3 + 4\cos\alpha + 8\cos^2\alpha\right)$.

The energy functional can be variationally minimized with respect to α similar to what was done for two-dimensional vortex defect (see Appendix 3.9.5). In the case of $H = 0$ and $K_1 = 0$, the problem boils down to a single dimensionless model parameter $g = \frac{\lambda}{\sqrt{K_2 J}}$ since the constants J, J_z and K_2 can be omitted by rescaling in-plane and out-of-plane distances and energy, respectively. The g-critical value, at which the system undergoes transition to DWA state, is universal ($g_{\mathrm{cr}} = 4/\pi$). The non-divergent solution exists at large $g = 1.6g_{\mathrm{cr}}$ (see Fig. 3.10), and the solution is not stable anymore at $g \approx 1.56g_{\mathrm{cr}}$. The same understanding could be achieved with use of scaling analysis of hyperbolic tangent profile, $F(r) = \pi \tanh(r/w)$. These stability

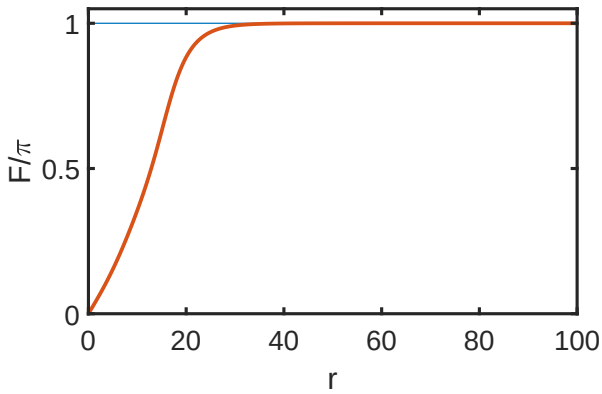

Figure 3.10: ***Optimized variational solution of three-dimensional Skyrmion*** *in the bulk Fe-langasite. The single dimensionless model parameter* $g = \frac{\lambda}{\sqrt{K_2 J}} = 1.6 g_{\rm cr}$.

arguments are universal because of the single dimensionless model parameter, g, which does not change under either energy or distances rescaling. However, the defect size can be rescaled only in z direction, which does not affect the contribution but exchange interactions. Consider $z = \Lambda_z z'$, then the spherical skyrmions in z' coordinates is an elongated 'needle' in the real space (z-coordinates). This 'needle' solution can be effectively examined by decreasing J_z to very small values, which gives minimal g-value of skyrmions stability: $g = 1.21 g_{cr}$ for $J_z = 0.01 J_{xy}$ Further relaxation of the 3D configuration would decrease this minimum value of g but our numerics shows that it still exceeds g_{cr} in the bulk material.

3.8 Outlook and Discussion

The importance of a larger order parameter space in triangular magnets with the 120° ordering for critical phenomena and topological defects was noted already some time ago [93]. An additional ingredient discussed in this paper is the lack of inversion symmetry in the crystal lattice, which gives rise to DM interactions resulting in additional long-period modulations of the 120° spin structure. The spin non-collinearity at the scale of one crystallographic unit cell gives rise to new magnetic phases and topological defects at a much larger length scale determined by the strength of the DM interactions.

We derived an effective model describing large-scale spin modulations in Fe-langasite, in particular the experimentally observed tilted spiral phase, and showed that the three-dimensional order parameter space of this non-collinear antiferromagnet allows for complex spin states and unconventional topological magnetic defects, such

as the coreless vortex tube and three-dimensional Skyrmion. The formal equivalence of the parameter spaces of antiferromagnets with a 120° spin ordering and superfluid ^{3}He-A calls for a study of magnetic analogs of the wealth of topological defects in the superfluid system [87, 88]. Note, however, that ^{3}He and the Skyrme model do not allow for Lifshitz invariants stabilizing nanosized topological defects in the chiral Fe-langasite.

There are other non-collinear antiferromagnets with frustrated exchange interactions that can host unusual topological defects, such as manganese nitrides with the cubic inverse perovskite crystal structure showing a variety of non-collinear spin structures and a giant negative thermal expansion effect [121–123], Pb_2MnO_4 with a non-centrosymmetric tetragonal crystal lattice and a rare 90° spin ordering [124], multiferroic hexagonal manganites with a trimerized triangular spin lattice and strongly coupled structural, ferroelectric and magnetic defects [125–127], swedenborgites with alternating triangular and Kagome spin lattices, which similar to Fe-langasite are both frustrated and non-centrosymmetric [108, 128], and the conducting non-collinear antiferromagnets, Mn_3Ge and Mn_3Sn, showing large anomalous Hall and Nernst effects and allowing for electric control of magnetic states [95–102, 129]. Matrix models are realizable within three-dimensional pyrochlore lattice [130] and potentially with the long-range physics of spiral states in helimagnets, where a zoo of screw dislocations has been recently predicted [131]. The unconventional topological defects discussed in this paper can be a new avenue of research in antiferromagnetic spintronics.

3.9 Appendix

3.9.1 Numerical simulations.

We re-write the energy of the effective model Eq. (3.7) in terms of the unit vectors, $\mathbf{V}_1$ and $\mathbf{V}_2$:

$$\begin{aligned}\mathcal{E} = &\frac{J_z}{2}\left[(\partial_z \mathbf{V}_1)^2 + (\partial_z \mathbf{V}_2)^2\right] + \frac{J_\perp}{2}\sum_{\mu=x,y}\left[(\partial_\mu \mathbf{V}_1)^2 + (\partial_\mu \mathbf{V}_2)^2\right] \\ &+ K_1(1-n_z) + \frac{K_2}{2}(1-n_z^2) - \frac{\chi}{2}(\mathbf{H}\cdot\mathbf{n})^2 \\ &- \lambda\sum_{i=1,2}\left[V_i^x \partial_y V_i^z - V_i^y \partial_x V_i^z\right] + J_{\rm ort}\left(\mathbf{V}_1\cdot\mathbf{V}_2\right)^2,\end{aligned} \tag{3.22}$$

where $\mathbf{n} = \mathbf{V}_1 \times \mathbf{V}_2$, and $\mathbf{V}_1$ and $\mathbf{V}_2$ are slowly varying vectors with Ψ replaced by ψ. The term with a large $J_{\rm ort} > 0$ is added to ensure the orthogonality of $\mathbf{V}_1$ and $\mathbf{V}_2$. We then discretize Eq. (3.22) and minimize energy by solving two coupled Landau-Lifshitz-Gilbert equations for the unit vectors $\mathbf{V}_1$ and $\mathbf{V}_2$ (effective spins) with an artificially large Gilbert damping.

3.9.2 Microscopic description of exchange interactions.

We first consider the exchange interactions between spin triangles stacked along the z direction parallel to the c axis

$$E_z = \sum_{m,\lambda}\Big[J_4\left(\mathbf{S}_{\lambda,m}\cdot\mathbf{S}_{\lambda,m+1}\right) + J_3\left(\mathbf{S}_{\lambda,m}\cdot\mathbf{S}_{\lambda+1,m+1}\right) + J_5\left(\mathbf{S}_{\lambda,m}\cdot\mathbf{S}_{\lambda-1,m+1}\right)\Big] \quad (3.23)$$

where $\lambda = (1,2,3)$ denotes the spin in a triangle ($\mathbf{S}_{\lambda+3,m} = \mathbf{S}_{\lambda,m}$) and m is the layer number. The exchange constants $J_3, J_4, J_5 > 0$ describe antiferromagnetic exchange interactions between the spin triangles in neighboring layers (see Fig.1 in the main text).

In terms of the vectors $\mathbf{V}_{1,m}$ and $\mathbf{V}_{2,m}$ describing the 120° spin ordering (see Eq.(1)), the energy reads

$$E_z = -\frac{3}{4}\sum_m\Big[A\left(\mathbf{V}_{1,m}\cdot\mathbf{V}_{1,m+1}+\mathbf{V}_{2,m}\cdot\mathbf{V}_{2,m+1}\right)+B\left(\mathbf{V}_{1,m}\cdot\mathbf{V}_{2,m+1}-\mathbf{V}_{2,m}\cdot\mathbf{V}_{1,m+1}\right)\Big] \quad (3.24)$$

where $A = J_3 + J_5 - 2J_4$ and $B = \sqrt{3}(J_5 - J_3)$.

From Eq.(1) we obtain

$$\begin{aligned}\mathbf{V}_1 &= \cos\Psi\,\mathbf{e}_\theta + \sin\Psi\,\mathbf{e}_\phi\,,\\ \mathbf{V}_2 &= -\sin\Psi\,\mathbf{e}_\theta + \cos\Psi\,\mathbf{e}_\phi\,,\end{aligned} \quad (3.25)$$

where

$$\begin{aligned}\mathbf{e}_\theta &= \frac{\partial\mathbf{n}}{\partial\theta} = (\cos\theta\cos\phi, \cos\theta\sin\phi, -\sin\theta)^T\,,\\ \mathbf{e}_\phi &= \frac{1}{\sin\theta}\frac{\partial\mathbf{n}}{\partial\phi} = (-\sin\phi, \cos\phi, 0)^T\,.\end{aligned} \quad (3.26)$$

The energy can then be written in the form

$$\begin{aligned}E_z = -\frac{3}{4}\sum_m\Big[&\left(A\cos\left(\Psi_{m+1}-\Psi_m\right) - B\sin\left(\Psi_{m+1}-\Psi_m\right)\right)\times\left(\mathbf{e}_{\theta,m}\cdot\mathbf{e}_{\theta,m+1}+\mathbf{e}_{\phi,m}\cdot\mathbf{e}_{\phi,m+1}\right)\\ &+\left(A\sin\left(\Psi_{m+1}-\Psi_m\right) - B\cos\left(\Psi_{m+1}-\Psi_m\right)\right)\times\left(\mathbf{e}_{\theta,m}\cdot\mathbf{e}_{\phi,m+1}-\mathbf{e}_{\phi,m}\cdot\mathbf{e}_{\theta,m+1}\right)\Big]\,.\end{aligned} \quad (3.27)$$

We can now get rid of the fast spin rotation by introducing the slowly varying ψ_m : $\Psi_m = Qcm + \psi_m$, where Q defined by $\tan Qc = -\frac{B}{A}$ is the wave vector of the fast-rotating spin spiral. Finally, we expand Eq.(3.27) in powers of gradients of the slowly varying ψ_m, $\mathbf{e}_{\theta,m}$ and $\mathbf{e}_{\phi,m}$, which gives the first term in the continuum model Eq.(3) given in the main text.

A similar procedure applied to exchange interactions between nearest-neighbor spin triangles in the ab layers

$$\begin{aligned} E_{xy} = J_2 \sum_{\mathbf{r}} \Big[& \mathbf{S}_1(\mathbf{r}) \cdot (\mathbf{S}_2(\mathbf{r}-\mathbf{a}-\mathbf{b}) + \mathbf{S}_3(\mathbf{r}-\mathbf{a}-\mathbf{b})) \\ & + \mathbf{S}_2(\mathbf{r}) \cdot (\mathbf{S}_1(\mathbf{r}+\mathbf{a}) + \mathbf{S}_3(\mathbf{r}+\mathbf{a})) \\ & + \mathbf{S}_3(\mathbf{r}) \cdot (\mathbf{S}_1(\mathbf{r}+\mathbf{b}) + \mathbf{S}_2(\mathbf{r}+\mathbf{b})) \Big] \end{aligned} \tag{3.28}$$

where $\hat{\mathbf{a}} = a\left(\frac{\sqrt{3}}{2}\hat{\mathbf{x}} + \frac{1}{2}\hat{\mathbf{y}}\right)$ and $\hat{\mathbf{b}} = a\left(-\frac{\sqrt{3}}{2}\hat{\mathbf{x}} + \frac{1}{2}\hat{\mathbf{y}}\right)$ are the basis vectors of the hexagonal lattice, a being the in-plane lattice constant, gives the second term in Eq.(3).

The covariant derivative $D_i\psi$ and $(\partial_i \mathbf{n} \cdot \partial_i \mathbf{n})$ are invariant under an arbitrary global rotation of spins due to the isotropic nature of Heisenberg exchange interactions. The rotational invariance is equivalent to invariance under $R \to OR$, where R is defined by Eq.(1) and O is an arbitrary SO(3) matrix. In terms of the slowly varying variables, the invariance of exchange interactions under rotation around the z axis through the angle α implies invariance under $\phi \to \phi + \alpha$ and the invariance under rotation around the y axis through the angle β ($|\beta| \ll 1$) implies invariance under $\theta \to \theta + \beta\cos\phi$, $\phi \to \phi - \beta\cot\theta\sin\phi$, $\psi \to \psi + \beta\frac{\sin\phi}{\sin\theta}$.

3.9.3 Lifshitz invariants.

The five independent LIs presented in the main text can be expressed in terms of $\mathbf{V}_1$ and $\mathbf{V}_2$:

$$\begin{aligned} L_1 &= X_1 \overleftrightarrow{\partial_x} Y_1 - X_2 \overleftrightarrow{\partial_x} Y_2 - X_1 \overleftrightarrow{\partial_y} Y_2 - X_2 \overleftrightarrow{\partial_y} Y_1 \\ L_2 &= 2Y_2 \overleftrightarrow{\partial_x} Z_2 - 2X_1 \overleftrightarrow{\partial_y} Z_1 + (X_2 + Y_1)\left(\overleftrightarrow{\partial_x} Z_1 - \overleftrightarrow{\partial_y} Z_2\right) \\ L_3 &= -X_1 \overleftrightarrow{\partial_x} Z_2 - Y_1 \overleftrightarrow{\partial_y} Z_2 + X_2 \overleftrightarrow{\partial_x} Z_1 + Y_2 \overleftrightarrow{\partial_y} Z_1 \\ L_4 &= X_1 \overleftrightarrow{\partial_y} Z_1 - Y_1 \overleftrightarrow{\partial_x} Z_1 + X_2 \overleftrightarrow{\partial_y} Z_2 - Y_2 \overleftrightarrow{\partial_x} Z_2 \\ L_5 &= X_1 \overleftrightarrow{\partial_x} X_2 - Y_1 \overleftrightarrow{\partial_x} Y_2 - X_1 \overleftrightarrow{\partial_y} Y_2 - Y_1 \overleftrightarrow{\partial_y} X_2 \end{aligned} \tag{3.29}$$

The last three survive the averaging over the fast spiral rotations along the c axis:

$$\begin{aligned} \langle L_3 \rangle &= \cos\theta\,(\sin\phi\,\partial_x\theta - \cos\phi\,\partial_y\theta - (\mathbf{n}\cdot\partial_\perp)\psi) \\ \langle L_4 \rangle &= \cos^2\theta\,(\sin\phi\,\partial_x\theta - \cos\phi\,\partial_y\theta) - (\mathbf{n}\cdot\partial_\perp)\psi \\ \langle L_5 \rangle &= \sin 2\phi \sin\theta\,\partial_x\theta - \cos 2\phi \sin^2\theta\,\partial_x\psi \\ &\quad + \cos 2\phi \sin\theta\,\partial_y\theta + \sin 2\phi \sin^2\theta\,\partial_y\psi \end{aligned} \tag{3.30}$$

The strongest interaction of this kind likely originates from the DMI between neighboring triangles in ab layers,

$$\begin{aligned}&\mathbf{D}_1\cdot\mathbf{S}_2(\mathbf{r})\times\mathbf{S}_1(\mathbf{r}+\mathbf{a}+\mathbf{b})+\mathbf{D}_2\cdot\mathbf{S}_3(\mathbf{r})\times\mathbf{S}_1(\mathbf{r}+\mathbf{a}+\mathbf{b})\\&+\mathbf{D}_3\cdot\mathbf{S}_1(\mathbf{r})\times\mathbf{S}_3(\mathbf{r}-\mathbf{b})+\mathbf{D}_4\cdot\mathbf{S}_2(\mathbf{r})\times\mathbf{S}_3(\mathbf{r}-\mathbf{b})\\&+\mathbf{D}_5\cdot\mathbf{S}_3(\mathbf{r})\times\mathbf{S}_2(\mathbf{r}-\mathbf{a})+\mathbf{D}_6\cdot\mathbf{S}_1(\mathbf{r})\times\mathbf{S}_2(\mathbf{r}-\mathbf{a})\end{aligned}\tag{3.31}$$

We first consider the interaction due to the y-component of $\mathbf{D}_1$ together with the symmetry-related interactions on the other bonds:

$$\begin{aligned}&\mathbf{D}_1=D_y\hat{\mathbf{y}}\quad\mathbf{D}_2=D_y\hat{\mathbf{y}}\\&\mathbf{D}_3=-D_y\hat{\mathbf{b}}\quad\mathbf{D}_4=-D_y\hat{\mathbf{b}}\\&\mathbf{D}_5=-D_y\hat{\mathbf{a}}\quad\mathbf{D}_6=-D_y\hat{\mathbf{a}}\end{aligned}\tag{3.32}$$

(the vectors $\mathbf{a},\mathbf{b},\mathbf{x}$ and $\mathbf{y}$ are defined in Fig. 1). In the continuum limit, these interactions give dominant L_4 included into the model given in the main text Eq.(3). The DMI resulting from $\mathbf{D}_1=D_x\hat{\mathbf{x}}$ and the symmetry related terms give 0 in the continuum limit after averaging over the fast rotations, whereas the interactions resulting from $\mathbf{D}_1=D_z\hat{\mathbf{z}}$ modify K_1.

In addition, there are 3 LIs favoring an additional modulation along the c axis: $\mathrm{Im}\left(R_+\overleftrightarrow{\partial_z}\overline{R}_+\right)$, $\mathrm{Im}\left(R_-\overleftrightarrow{\partial_z}\overline{R}_-\right)$, and $\mathrm{Im}\left(Z\overleftrightarrow{\partial_z}\overline{Z}\right)$, which can also be written in the form

$$\begin{aligned}L_1^z&=X_1\overleftrightarrow{\partial_z}Y_1+X_2\overleftrightarrow{\partial_z}Y_2\\L_2^z&=X_2\overleftrightarrow{\partial_z}X_1+Y_2\overleftrightarrow{\partial_z}Y_1\\L_3^z&=Z_2\overleftrightarrow{\partial_z}Z_1\end{aligned}\tag{3.33}$$

Averaging over fast rotations, we obtain

$$\begin{aligned}\langle L_1^z\rangle&\simeq(1+\cos^2\theta)\,\partial_z\phi+2\cos\theta\,\partial_z\psi\\\langle L_2^z\rangle&\simeq 2\cos\theta\,\partial_z\phi+(1+\cos^2\theta)\,\partial_z\psi\\\langle L_3^z\rangle&\simeq\sin^2\theta\,\partial_z\psi\end{aligned}\tag{3.34}$$

3.9.4 Field-induced phase transitions.

The transition line between the low-field uniform state with $n\|z$ and the high-field DH state in which $\mathbf{n}$ rotates continuously in the xz towards the magnetic field $H\|x$

$$h_{\mathrm{R}}^2=|k_1|+k_2-1\tag{3.35}$$

was obtained in the main text (above Eq.(5)). Here h is the dimensionless magnetic field defined by $\chi H^2=h^2\frac{\lambda^2}{2J}$ and $k_{1,2}$ are dimensionless anisotropy parameters: $k_i=K_i/\left(\frac{\lambda^2}{2J}\right)$, $i=1,2$.

At the transition line separating the uniform and DWA states the energy of the domain wall, across which θ increases by 2π along the y direction ($\phi = \pi/2$), is 0. An equation for the domain wall is obtained by minimizing Eq.(4) and its first integral has the form

$$\frac{J_\perp}{2}\left(\frac{d\theta}{dy}\right)^2 - U(\theta) = V \tag{3.36}$$

where

$$U(\theta) = K_1(1-\cos\theta) + \frac{K_2}{2}(1-\cos^2\theta) \tag{3.37}$$

and V is a constant. At the transition line, $V = 0$ and the domain wall energy is

$$E_{\rm DW} = \int_0^{2\pi} \sqrt{2J_\perp U(\theta)}\, d\theta - \pi\lambda = 0 \tag{3.38}$$

Calculation of the integral gives an equation for the critical curve, $h_{\rm c1}(k_1)$:

$$\sqrt{k_2 - h_{\rm c1}^2}\left(\sqrt{1+g} + \frac{g}{2}\ln\frac{2+g+2\sqrt{1+g}}{g}\right) = \frac{\pi}{2\sqrt{2}} \tag{3.39}$$

where $g = \frac{|k_1|}{k_2 - h_{\rm c1}^2}$.

For $H > H_{\rm c1}$, $V \neq 0$ and the domain wall energy

$$E_{\rm DW} = \int_0^{2\pi} \sqrt{2J_\perp(U(\theta)+V)}\, d\theta - \pi\lambda - VL < 0 \tag{3.40}$$

where L is domain wall length, which in the DWA state is finite and given by

$$L = \sqrt{\frac{J_\perp}{2}}\int_0^{2\pi} \frac{d\theta}{\sqrt{U(\theta)+V}} \tag{3.41}$$

(see Eq.(3.36)). Minimizing the average energy density, $\frac{E_{\rm DW}}{L}$, with respect to V, we obtain

$$\int_0^{2\pi} \sqrt{2J_\perp(U(\theta)+V)}\, d\theta = \pi\lambda \tag{3.42}$$

and

$$\frac{E_{\rm DW}}{L} = -V \tag{3.43}$$

At the critical field $H_{\rm c2}$, the average energy density of the DWA state equals that of the uniform spiral state:

$$-V = U(\theta_{\rm R}) - \frac{\chi H_{\rm c2}^2}{2}\sin^2\theta_{\rm R} \tag{3.44}$$

where $\theta_{\rm R}$ is given by Eq.(5). Solving Eq. (3.42) with V given by Eq.(3.44), we obtain the $h_{\rm c2}(k_1)$ line. The phase boundaries discussed in this section are plotted with solid black lines in Fig. 3.

3.9.5 Two-dimensional topological defect.

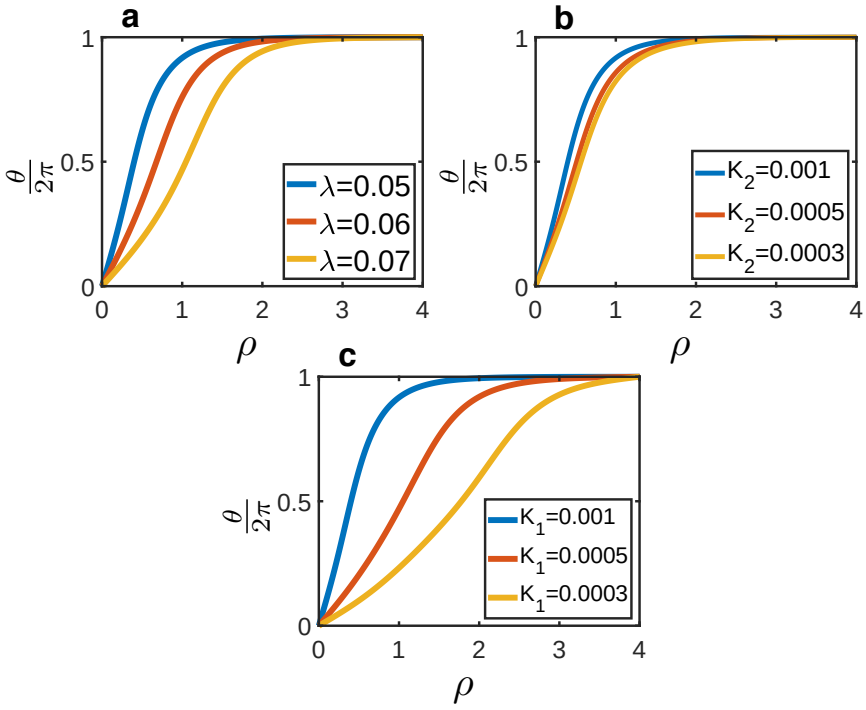

Figure 3.11: ***One dimensional profile of the coreless vortex.*** *$\theta(\rho)$ for* **a** *three values of λ and $K_1 = K_2 = 10^{-3}$,* **b** *three values of K_2, $K_1 = 10^{-3}$ and $\lambda = 0.05$, and* **c** *three values of K_1, $K_2 = 10^{-3}$ and $\lambda = 0.05$. ρ is measured in units of $\frac{\lambda}{K_1}$.*

In zero applied magnetic field, the 2D topological defect has rotational symmetry: $\theta = \theta(\rho)$, $\phi = \varphi + \frac{\pi}{2}$ and $\psi = -\varphi$. The energy of the defect [see Eq.(3) in the main text] counted from the energy of the spiral state with $\mathbf{n} \| \hat{\mathbf{z}}$ state is

$$E = 2\pi \int \rho \, d\rho \Big\{ \frac{J_\perp}{2} \Big[(\partial_\rho \theta)^2 + \frac{1}{\rho^2} \left(\sin^2\theta + 2(1-\cos\theta)^2 \right) \Big] + K_1(1-\cos\theta) + \frac{K_2}{2} \sin^2\theta - \lambda \Big[\cos^2\theta \, \partial_\rho \theta + \frac{\sin\theta}{\rho} \Big] \Big\} \tag{3.45}$$

Figure 3.11 shows $\theta(\rho)$ found by numerical minimization of Eq.(3.45) with the boundary conditions, $\theta(0) = 0$ and $\theta(\infty) = 2\pi$, for various values of K_1 and K_2. The soliton radius is independent of $J_\perp$ due to the scaling invariance of the exchange energy in two spatial dimensions and is determined by the relative strength of λ and anisotropy parameters.